scientific reports

Check for updates

OPEN

Experimental study on the influence of ground temperature and pore water pressure on the mechanics of excavation unloading sandstone

Sheng Gong, Lili Chen, Xingzhou Chen✉ & Zhenhan Li

As tunnel engineering in western China advances deeper underground, it encounters increasing issues of high ground temperature and high water pressure. To study the mechanical properties of unloading sandstone under the combined effects of temperature and pore water pressure, triaxial unloading and reloading experiments were conducted on sandstone under different temperatures, pore water pressures, and confining pressures. The results showed: (1) The peak strength of unloading sandstone decreases with increasing temperature and pore water pressure. The elastic modulus of unloading sandstone increases with temperature but decreases with increasing pore water pressure. (2) The influence of pore water pressure on the unloading deformation of sandstone has a threshold. At low pore water pressure (1 MPa), temperature has little effect on the deformation of unloading sandstone. At medium to high pore water pressures (2, 3 MPa), temperature-induced unloading softening characteristics are obvious. (3) SEM images show that with increasing temperature, the number and width of microcracks in the rock increase. With increasing pore water pressure, rock cohesion decreases and friction angle increases; under 3 MPa water pore pressure, rock cohesion decreases by 24.8%. (4) The rock's energy storage capacity decreases with increasing temperature and pore water pressure. At high pore water pressure (3 MPa), the effect of temperature on the dissipation energy of sandstone is more significant. In addition, as the temperature rises, the proportion of elastic energy at the rock's peak increases, while the proportion of dissipation energy decreases.

In recent years, with the rapid development of the economy, engineering construction, and energy exploitation have gradually gone deep; it is necessary to consider the impact of temperature on the mechanical strength of unloading surrounding rock in the construction of deep-buried tunnels, deep oil and gas extraction, geothermal energy development, underground coal gasification, and other projects. Particularly in the Southwest region of China, where the distribution of geothermal flow is anomalous[1] presenting significant challenges due to high ground temperature and high water head, many tunnel constructions[2–4], such as the Bangfu tunnel[5] and Sangzhuling tunnel[6], have encountered the challenge of high ground temperature. And as the burial depth increases, the water head pressure in the rock layers also increases, with sudden water and mud inflows particularly prominent. The Jinping II Hydropower Station diversion tunnel[7] and the Songlin tunnel[8] encountered high pressure water surges during construction. In addition, excavation unloading disturbance is the primary cause of deformation and instability in the rocks surrounding deep tunnels[9,10]. Therefore, it is important to study the mechanical characteristics of unloading rock under high pore water pressure and high ground temperature environments for the stability evaluation of underground engineering surrounding rock.

In underground engineering construction, the effects of stress, geothermal temperature, and groundwater on rock masses are common. Many scholars have studied the physical and mechanical properties of rocks under the influence of these three factors. In the study of hydro-mechanical coupling, Xiao et al.[11] and Zhang

School of Architecture and Civil Engineering, Xi'an University of Science and Technology, Xi'an 710054, China. ✉email: xzchen0416@xust.edu.cn

et al.[12] conducted hydro-mechanical coupling tests and found that as water pressure increases, the axial strain continuously decreases, while the radial strain and volumetric strain exhibit an evolution characterized by first increasing and then decreasing. Liu et al.[13] further pointed out that as water pressure increases, the micropores in rocks gradually transform into mesopores and macropores, leading to an overall increase in rock porosity. Ma et al.[14] conducted uniaxial compression tests on fractured rock under water-saturated conditions, indicating that water-saturated samples had more secondary cracks and significantly lower fracture strength than dry samples. Meanwhile, Xiao et al.[15] demonstrated through triaxial tests on fractured rock that water pressure accelerates wing crack propagation while suppressing the development of secondary cracks. In the study of thermo-mechanical coupling experiments, Keshavarz et al.[16], Pathiranagei et al.[17], and Qin et al.[18] investigated the mechanical properties of rocks after exposure to high temperatures (above 800 °C). The study indicated that as the temperature increased, rock strength decreased while strain increased, with high-temperature rocks exhibiting significantly enhanced ductility. Rao et al.[19] and Kumari et al.[20] conducted mechanical tests on rocks under real-time high temperature conditions, noting that the tensile cracks and axial splitting failure characteristics of rocks were pronounced under real-time high temperature conditions. Zuo et al.[21] also pointed out that the primary cracks in rock close at 25–150 °C, indicating that thermal effects at lower temperatures help enhance the rock strength. In engineering projects, the combined effects of stress, temperature, and water are often encountered, which significantly increases engineering risks.

To study the mechanical properties and microscopic changes of rocks under thermo-hydro-mechanical coupling (T-H-M), Lu et al.[22] conducted uniaxial tests on mudstone and sandstone under water bath heating conditions. They found that with increasing temperature, the uniaxial strength and elastic modulus of sandstone increased, while those of mudstone decreased. Meng et al.[23] pointed out, based on T-H-M experiments, that the change in sandstone porosity under real-time high temperature conditions below 400 °C is smaller than the porosity of sandstone after heat treatment. Bao et al.[24] investigated the mechanical properties of sandstone under T-H-M coupling, finding that the mechanical parameters of sandstone first decreased and then increased with rising temperature. Zhu et al.[25] also found similar patterns in tests conducted at higher temperatures. Li et al.[26] discussed the effects of pore water pressure and temperature on the uniaxial strength and pore structure of rocks, emphasizing that high pore water pressure significantly impacts rock permeability. Xu et al.[27] further pointed out that under T-H-M coupling conditions, the mechanism of permeability reduction is primarily caused by the thermal expansion of illite, as well as pore filling and throat blockage effects induced by newly released particles. Li et al.[28,29] developed a DEM model based on the coupling of T-H-M to simulate the cross-scale failure of small rock samples during compression loading. Lei et al.[30] and Zhang et al.[31] constructed a THM damage model to simulate the stress, deformation, seepage, and heat conduction of engineering fractured rock masses under thermal-hydraulic-mechanical coupling conditions. In addition, the surrounding rock of underground engineering has suffered excavation unloading damage. Under unloading conditions, the stress, deformation, and failure characteristics of rocks differ significantly from those of in-situ rocks[32]. Kang et al.[33] and Xiao et al.[34] conducted mechanical unloading tests on rocks after high temperature exposure, and their studies indicated that rock failure during the unloading stage is caused by intense radial deformation and volumetric shear dilation. However, research on the mechanical properties of unloading rocks under the combined effects of temperature and pore water pressure remains scarce.

Previous studies primarily investigated the mechanical properties of rocks under high temperatures (above 100 °C); however, the high ground temperature problems faced in engineering construction are often below 100 °C. Additionally, engineering rock masses are subjected to excavation unloading disturbances, which significantly impact rock strength and deformation, and past research has paid limited attention to the unloading effects experienced by engineering rock masses. Therefore, in this paper, triaxial unloading and reloading tests were carried out on sandstone under different ground temperatures, water pressures, and peripheral pressures, which can be used as a reference for the engineering design and disaster prevention of rocky tunnels under the environments of high ground temperatures and high water pressures.

Materials and methods
Materials and sampling
The sandstone used in this experiment was taken from the high-temperature section of a water diversion tunnel in Yunnan, China. According to the specifications, the samples were processed into cylindrical samples with a diameter of 50 mm and a height of 100 mm, with the diameter and height error not exceeding 0.3 mm. The average dry density of the samples was 2.36 g/cm³; the average saturated porosity was 9.49%, and the average P-wave velocity was 2.83 km/s. Samples with significant deviations in mass, porosity, and P-wave velocity from the average values were excluded. The sandstone location and representative sample are shown in Fig. 1.

X-ray diffraction tests were conducted on sandstone. Based on the mineral X-ray diffraction patterns, qualitative interpretation and semi-quantitative analysis of the minerals were performed. Figure 2 shows the XRD results; the main mineral components detected in the red sandstone are quartz (57.6%), microcline (16.9%), calcite (15.3%), and clinochlore (8.4%), along with minor amounts of pyrite (1.3%) and albite (0.5%).

The fresh rock is reddish-brown and has a blocky structure. Figure 3a shows the sandstone rock samples under a polarizing microscope. The rock is composed of terrigenous sand, with a small amount of terrigenous silt, clay, calcite, and hematite. The terrigenous sand consists of feldspar, quartz, and a small number of rock fragments, exhibiting subangular to angular shapes, with sizes ranging from 0.06 to 0.23 mm. The terrigenous silt is composed of quartz and a small amount of feldspar, with sizes ranging from 0.02 to 0.06 mm. The clay appears in a micro-flaky and cryptocrystalline form, with sizes less than 0.01 mm, filling the spaces between the terrigenous sand grains. Calcite occurs in a granular form, with sizes ranging from 0.02 to 0.1 mm. Hematite appears in cryptocrystalline and dust-like form.
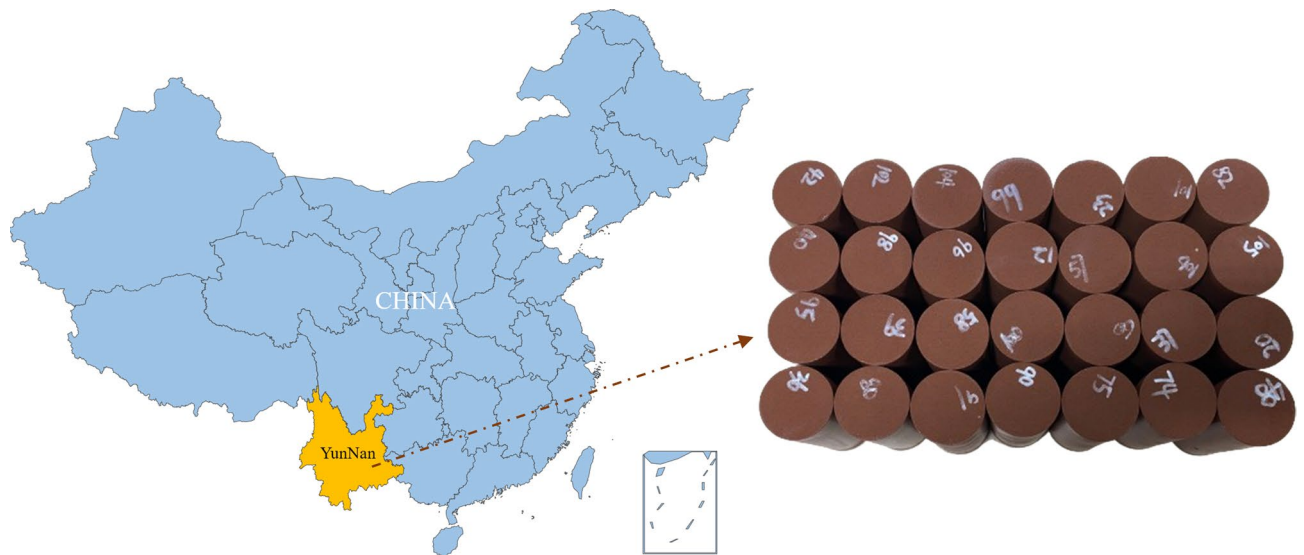
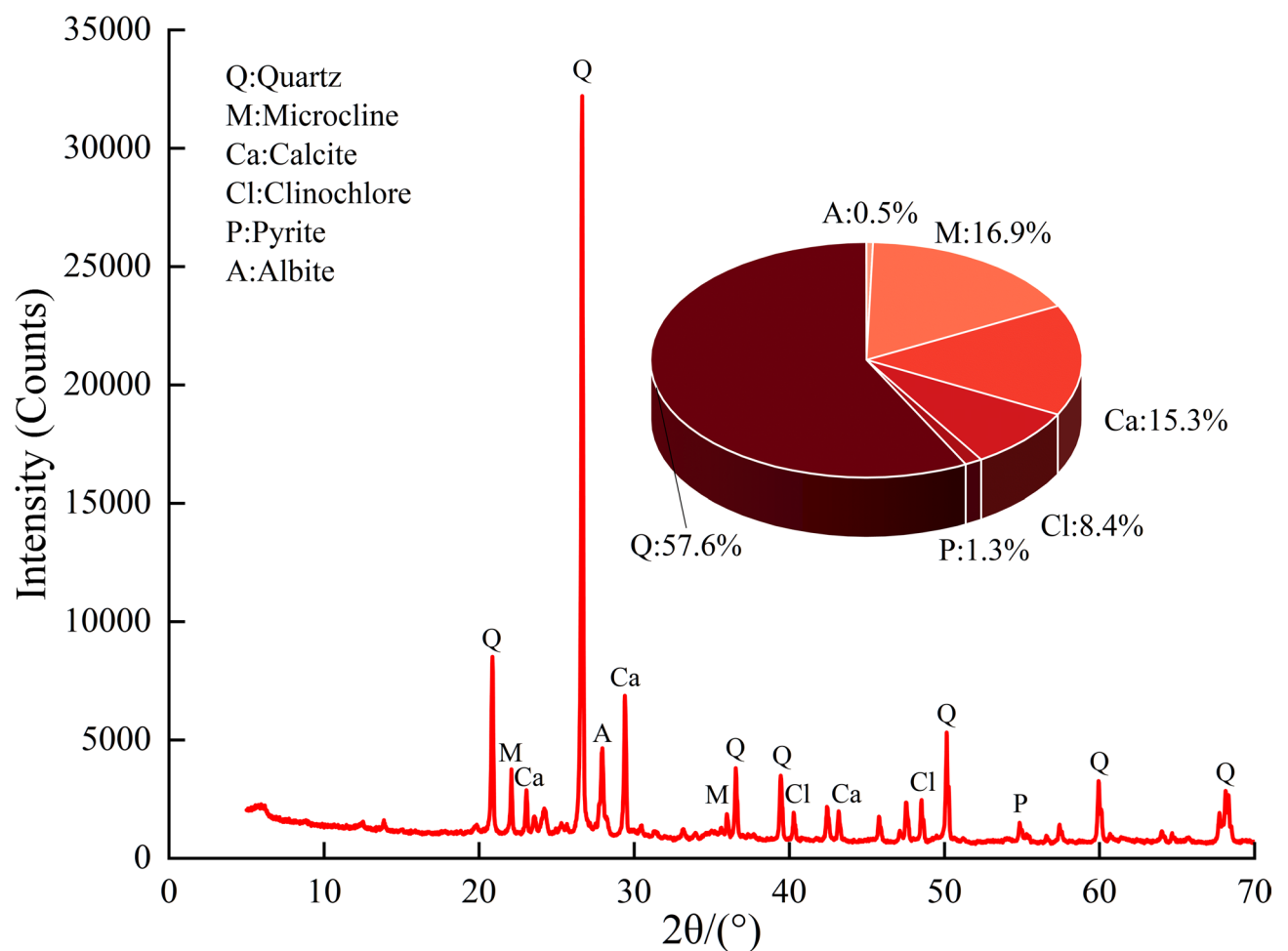**Fig. 1**. Sandstone location and typical sandstone sample (Software: QGIS, Version: 3.18.2, URL: https://qgis.org/en/site/).

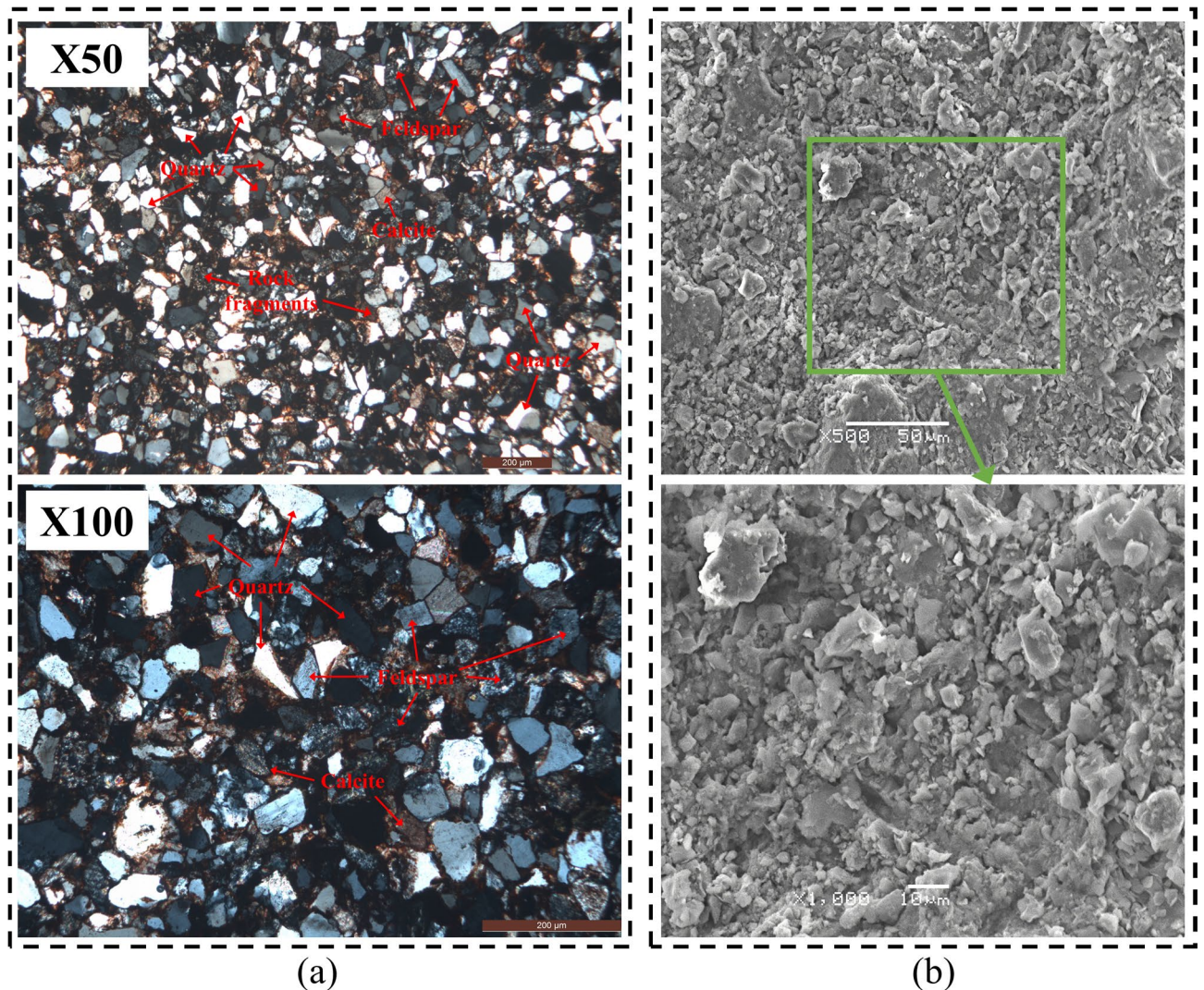**Fig. 2**. XRD diffraction pattern and components of this sandstone.

Fig. 3. Sandstone microscopic image: (**a**) Polarized microscopy results; (**b**) SEM photomicrographs.

The electron microscopic image of the sandstone in Fig. 3b shows that the shape of the sandstone particles is not smooth; most of the particles have angular edges and relatively rough surfaces, which may be caused by the collision and friction between the grains during the sedimentation process, and some pores can also be observed between the grains.

The experiments were carried out using the THMC (Thermal-Hydraulic-Mechanical-Chemical) multi-field coupled triaxial rheological testing system, which is equipped with axial and circumferential deformation measurement devices and a temperature control component. Before the mechanical experiment, the rock P-wave velocity and mass parameters were tested. The main experimental equipment is shown in Fig. 4.

Test process

To replicate the in-situ stress, temperature, and pore water pressure conditions of rocks. The experimental stress conditions were set at three confining pressures: 10, 15, and 20 MPa. Considering the geothermal gradient, two ground temperatures of 40 °C and 55 °C were selected, with 25 °C as the control group, and the experimental seepage pressures were set at three pore water pressures: 1, 2, and 3 MPa. The experimental scheme is as follows:

① Triaxial compression test: Saturated rock samples were subjected to triaxial compression tests under confining pressures of 10, 15, and 20 MPa to determine the peak compressive strength of the rock samples under different confining pressure conditions.

② Triaxial unloading test: Saturated rock samples were submitted to triaxial unloading tests under confining pressures of 10, 15, and 20 MPa. The axial pressure was loaded to 70% of the sample's peak strength under each confining pressure as the starting point for unloading the confining pressure. Permitted the calculation of the confining pressure values at unloading failure under different confining pressures, thus establishing the maximum removable confining pressure, as indicated in Table 1. To model the unloading damage of rock
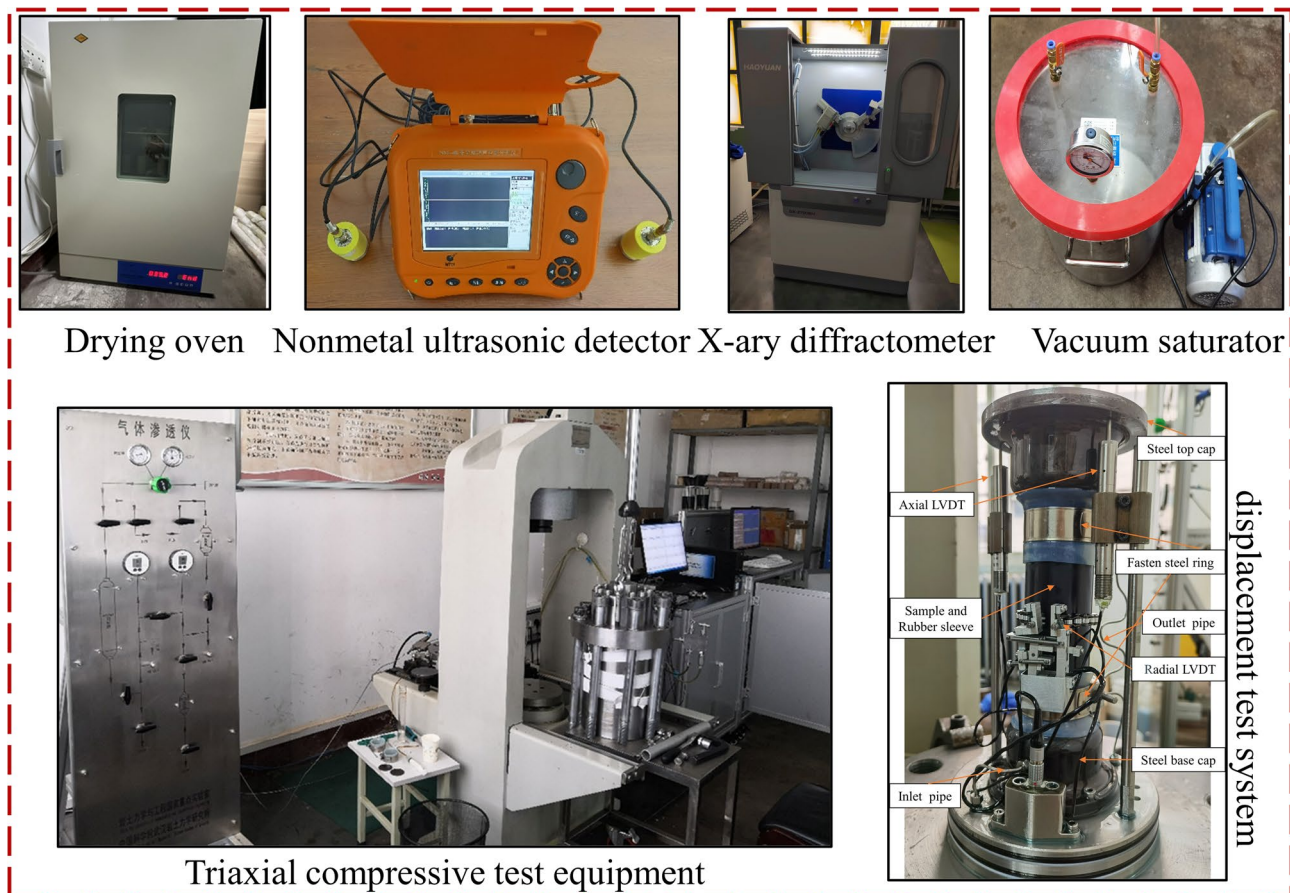
Fig. 4. Experimental equipment.

Confining pressure/(MPa)	Peak strength/(MPa)	Unloading failure confining pressure/(MPa)	Notes
10	113	–	
10	–	3	Axial Pressure 79.1 MPa, Constant Axial Pressure Unloading
15	140	–	
15	–	5.4	Axial Pressure 98.0 MPa, Constant Axial Pressure Unloading
20	152	–	
20	–	8	Axial Pressure 106.4 MPa, Constant Axial Pressure Unloading

Table 1. Triaxial loading and unloading strength.

mass during excavation, the unloading amount was introduced to represent different degrees of unloading damage[9]. The unloading amount M is defined as follows:

$$M = \frac{\left(\sigma_3^0 - \sigma_3^i\right)}{\left(\sigma_3^0 - \sigma_3^f\right)} \times 100\% \tag{1}$$

where M represents the amount of confining pressure unloading, σ_3^0 represents the initial confining pressure, σ_3^i represents the target value for confining pressure unloading, and σ_3^f represents the confining pressure at the time of unloading failure.

To ensure that the rock samples with unloading damage are usable for engineering purposes, subsequent experiments focused on rock samples with an unloading amount of 60%.

③ Triaxial unloading test with thermal-hydro coupling: Wrap the heating element around the pressure chamber's surface to begin heating it after the saturated rock sample has been installed. Once the rock sample reaches the target temperature, continue it for 2 h to ensure uniform heating. The test stress path is shown in Fig. 5. Apply confining pressure to a predetermined value (10, 15, 20 MPa) and pore water pressure (1, 2,
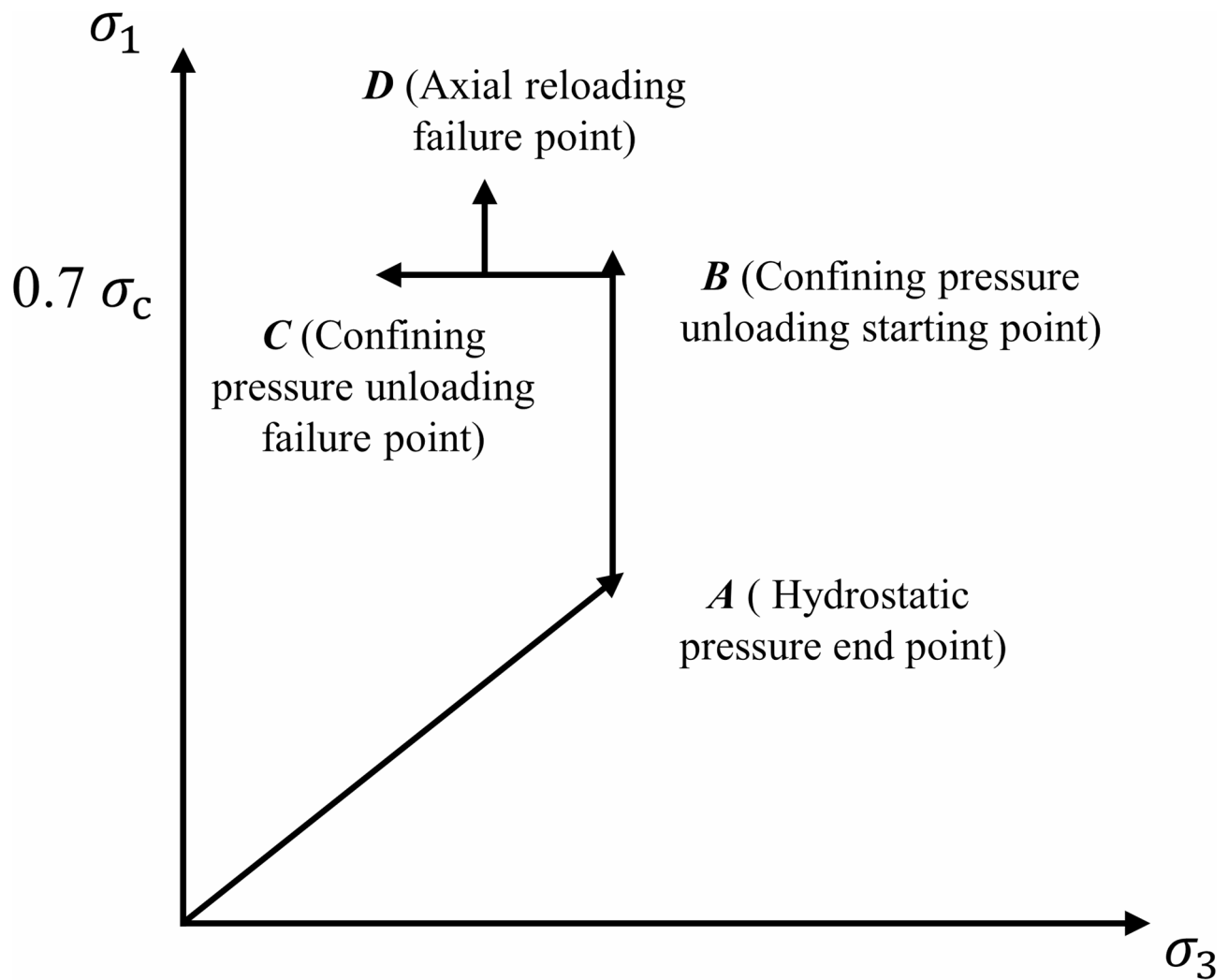
Fig. 5. Stress path diagram.

3 MPa) to reach point (A) After the confining pressure and pore water pressure stabilize, apply axial pressure at a loading rate of 4 MPa/min to 70% of the triaxial compressive strength, reaching point (B) Keep the axial stress constant and unload the confining pressure at a rate of 1 MPa/min to 60% of the maximum unloadable confining pressure. Finally, maintain the confining pressure constant and add axial pressure to the sample until failure, reaching point D.

Experimental results
Stress–strain curve
The deviatoric stress-strain curves of the rock samples are show in Fig. 6; experimental results show that confining pressure is a critical factor affecting the strength and deformation of rock samples. Under the same temperature and pore water pressure conditions, rock samples subjected to greater confining pressure exhibit higher peak strengths upon reloading, as well as greater axial and lateral deformation. At a high confining pressure of 20 MPa, the rock sample is subjected to strong lateral constraints, which hinder the development of internal fractures, and the stress-strain curve of the rock sample during the unloading stage is approximately linear. However, under medium to low confining pressures (10, 15 MPa), the lateral restraint on the rock is lessened, and pore water pressure reduces the effective stress on the rock, leading to a decrease in the strength of the cementing material and an increase in interparticle slip. A further reduction during the unloading stage accelerates the development of microcracks. Water can then more fully interact with the parent rock particles, causing rock softening and the further opening of unloading cracks.

Figure 7 shows that when the pore water pressure is the same, the elastic modulus of the rock samples increases with rising temperature (calculated in this study based on the slope of the linear segment of the axial stress–strain curve of the rock samples), while the peak stress exhibits a decreasing trend. This may be because the energy generated by the heating of mineral particles enhances their resistance to external deformation; at
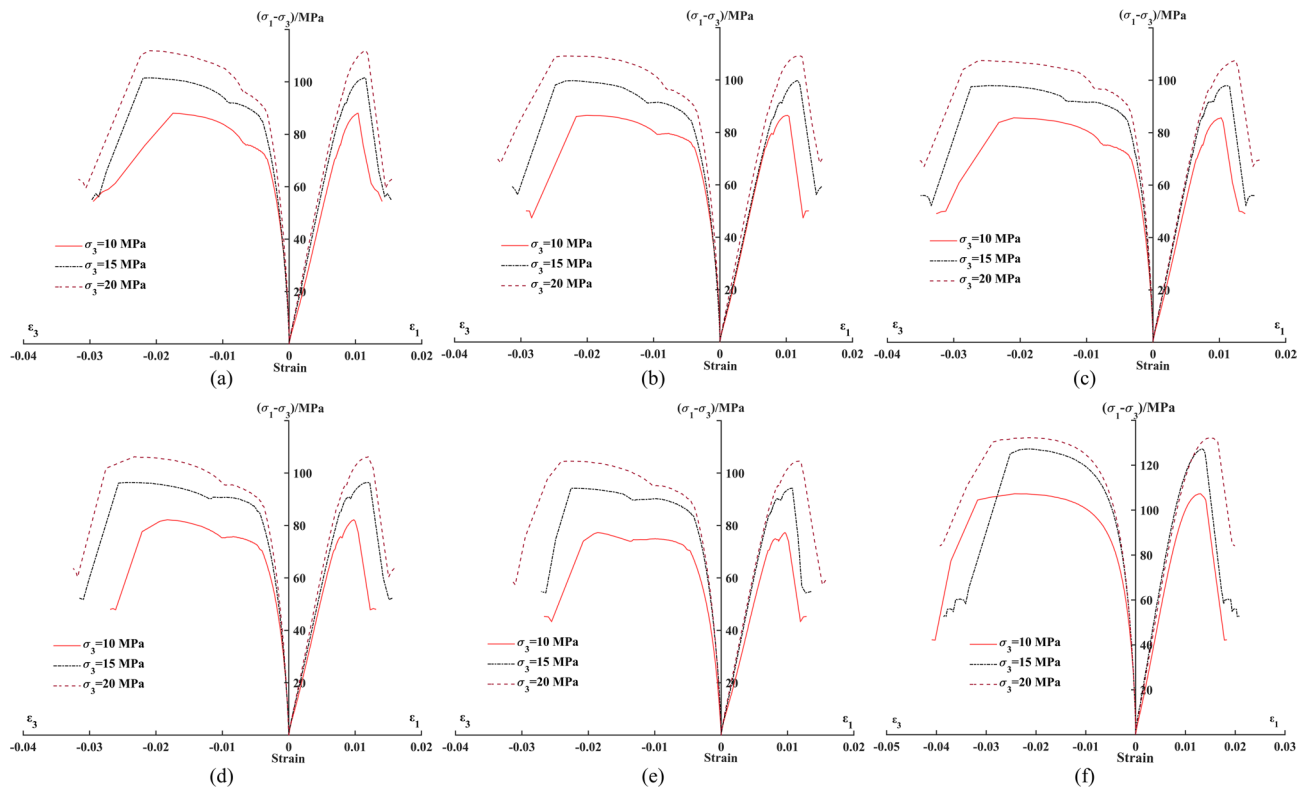
Fig. 6. Stress–strain curves under different temperatures and pore water pressure.
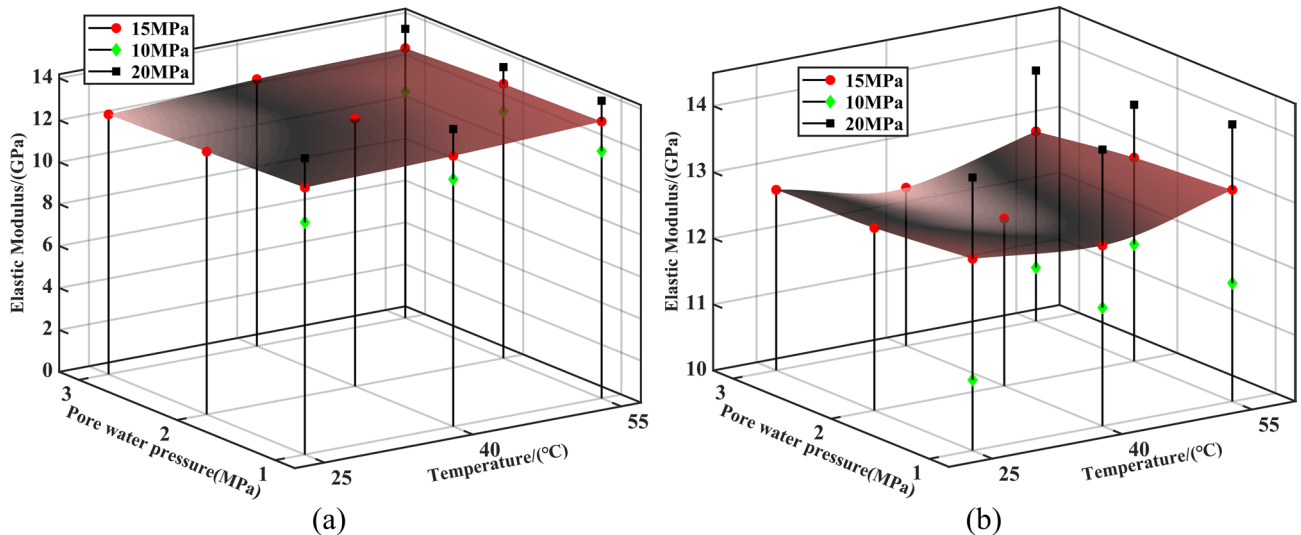

Fig. 7. Mechanical properties of samples at different confining pressures, temperatures, and pore water pressures: (**a**) Elastic modulus; (**b**) Peak stress.

relatively low temperatures, the propagation of microcracks is suppressed[35], leading to an increase in the elastic modulus of the rock samples during the initial loading stage. However, due to the tiny temperature change range, the rise is not significant. Nevertheless, as sandstone contains distinct mineral particles with differing coefficients of linear expansion, the rock matrix exhibits anisotropy. The temperature rise causes weakening at the edges of mineral crystals[36], resulting in a reduction of the rock's peak strength.

Under the same confining pressure and temperature conditions, it becomes clear that the elastic modulus and peak stress of the rock sample decrease as the pore water pressure increases. The external load causes changes in the rock skeleton, compressing or stretching the pore space used for water storage; during the experiment, the rock is in an environment of high pore water pressure. When the volume of pore space is smaller than the volume

of pore water, the incompressibility of water forces the entrapped water to flow. Given that the connectivity of the internal pores is poor. Compressed pore water will therefore cause an increase in local pore water pressure. For the pores themselves, water pressure acts as a tensile stress, which exacerbates the stress concentration at the tips of the holes (cracks), further promoting pore expansion to increase their volume to reduce local pore water pressure. These microscopic processes lead to a decay in the macroscopic mechanical properties of the rock. Furthermore, the presence of clay minerals may also affect the elastic modulus of water-bearing sandstone[37].

Deformation characteristics of sandstone

To quantitatively analyze the effect of temperature and pore water pressure on the deformation characteristics of rock samples during the unloading damage process, the concept of strain-confining pressure compliance[12] is introduced. It is expressed as the ratio of the strain increment caused by unloading confining pressure to the reduction in confining pressure Eq. (2). This physical quantity represents the rate of change in axial or circumferential deformation with changes in confining pressure. The strain-confining pressure compliance indicates the rate at which the internal structure of the rock sample responds to changes in confining pressure, with higher strain-confining pressure compliance indicating a greater sensitivity of the deformation direction to unloading.

$$\Delta\dot{\varepsilon}_i = \frac{\Delta\varepsilon_i}{\Delta\sigma_3} \tag{2}$$

where $\Delta\dot{\varepsilon}_i$ represents the strain-confining pressure compliance (where $i = 1, 3$ represent axial and circumferential strain, respectively); $\Delta\varepsilon_i$ represents the strain increment (where $i = 1, 3$ represent axial and circumferential strain, respectively); $\Delta\sigma_3$ represents the change in confining pressure.

Under a confining pressure of 15 MPa, strain-confining pressure compliance during the unloading stage is depicted in Fig. 8. The slight rise in axial strain-confining pressure compliance under ground temperature conditions at 1 MPa pore water pressure indicates that unloading rock samples are less sensitive to temperature at low pore water pressure. However, under medium to high pore water pressures (2, 3 MPa), the lateral strain-confining pressure compliance increases significantly with temperature, and the rate of increase in lateral strain-confining pressure compliance is much higher than that in the axial. At a pore water pressure of 3 MPa and temperatures of 40 °C and 55 °C, the axial strain-confining pressure compliance of the rock samples increased by 18.2% and 70.5%, while lateral strain-confining pressure compliance increased by 93.2% and 132.5%. This indicates that the coupling effect of high pore water pressure and high ground temperature intensifies damage to the rock mass during unloading, reducing lateral constraints, and leads to particle slip and dislocation within the rock, and is accompanied by the formation of microcracks. The influence of temperature on the macroscopic mechanical behavior of the rock causes thermal stress and crack generation[38]. This creates pathways for water pressure intervention, which further exacerbates unloading crack expansion, leading to increased rock fractures and significant axial and lateral deformation during unloading. A threshold effect exists for pore water pressure impact on deformation, with temperature softening effects becoming evident only at high pore water pressures.

Figure 9 shows the relationship between strain-confining pressure compliance and confining pressure during unloading under high ground temperature (55 °C). Under varying confining pressures, both the axial and lateral strain-confining pressure compliance of the rock samples increase with rising pore water pressure, while the confining pressure significantly inhibits deformation during the unloading stage. At high confining
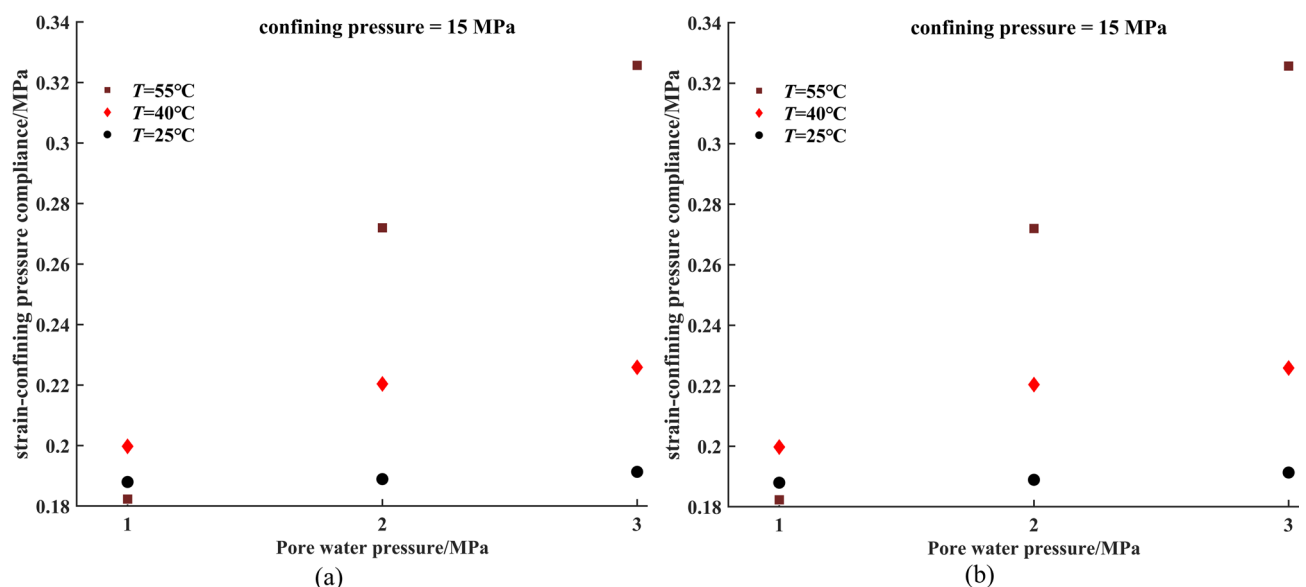

Fig. 8. Relationship between the strain-confining pressure compliance and the pore water pressure under different temperatures: (**a**) Axial; (**b**) Circumferential.
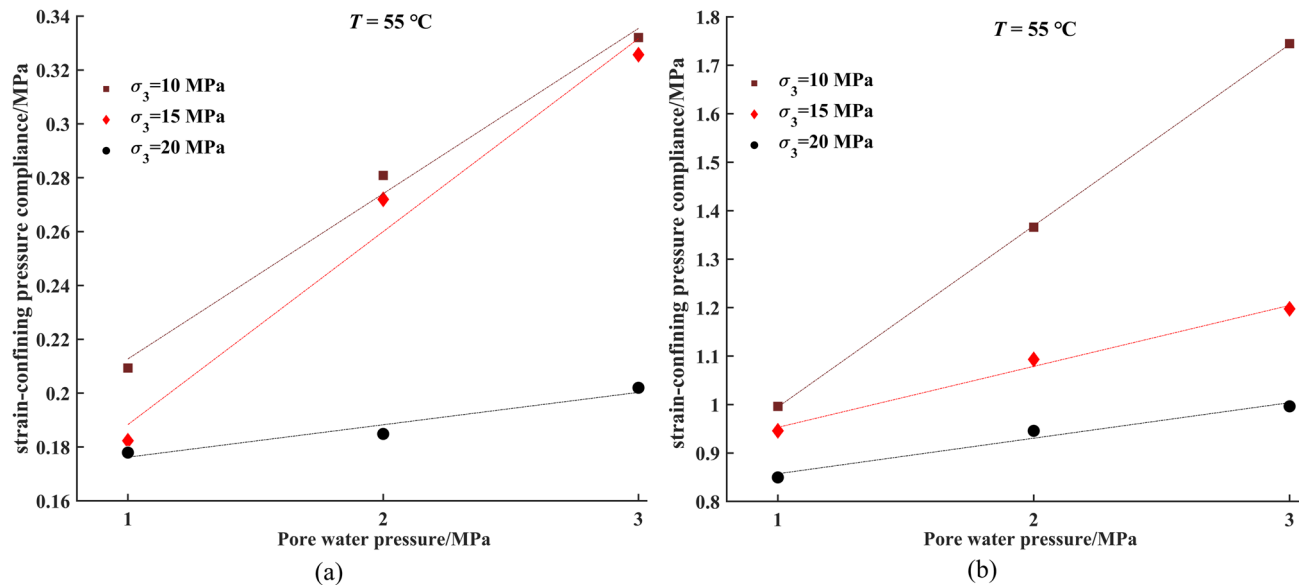
Fig. 9. Relationship between the strain-confining pressure compliance and the pore water pressure under different confining pressures: (**a**) Axial; (**b**) Circumferential.

pressure (20 MPa), the axial and lateral strain confining pressure compliances increase gradually with pore water pressure. Under medium and low confining pressures (10, 15 MPa), both the lateral and axial strain-confining pressure compliance exhibit a pronounced growth trend during unloading.

It is evident that the deformation of unloading rock samples is sensitive to changes in confining pressure; confining pressure serves to inhibit deformation and shear slippage damage in the samples. Samples under high confining pressure exhibit a gradual increase in axial strain-confining pressure compliance during the unloading stage. In contrast, under medium to low confining pressure conditions, the elevated ground temperature environment leads to an expansion in the internal mineral particle gaps of the rock, providing pathways for pore water pressure intervention. This seepage effect intensifies deformation during the unloading stage[11,39,40].

Shear strength parameters

The failure mode upon reloading of unloading rock samples is chiefly shear failure. Shear parameters can be derived from the Mohr-Coulomb failure envelope, with the shear strength parameters mainly comprising cohesion c and internal friction angle φ, calculated using Eqs. (3) and (4) to determine changes in shear strength parameters with temperature and pore water pressure.

$$\sigma_1 = k\sigma_3 + q \tag{3}$$

$$\varphi = \arcsin \frac{(k-1)}{(k+1)}, \ c = \frac{1-\sin\varphi}{2\cos\varphi} \tag{4}$$

where: k and q are the slope and intercept of linear fitting; c and φ are the cohesion and the friction angle.

The Mohr–Coulomb envelopes under different temperatures and water pressures are shown in Fig. 10, In high-ground temperature conditions, the cohesion of rock samples decreases with the rise in pore water pressure; as pore water pressure increases from 1 MPa to 3 MPa, with cohesion reductions of 10.9% and 24.8%; the increase in pore water pressure weakens the intergranular cement, diminishing adhesion and thereby cohesion. Concurrently, the internal friction angle of rock samples increases with the rise in pore water pressure, as pore water pressure increases from 1 MPa to 3 MPa, the friction angle increases by 5.7% and 13.1%. The changes and trends in the internal friction angle with increased pore water pressure are more pronounced than those in cohesion, primarily due to particle sliding friction and the interlocking effect between rough surfaces. The rise in pore water pressure decreases cohesion, leading to the earlier manifestation and exacerbation of wear on fracture surfaces.

Additionally, the lubricating effect of pore water makes the fault gouge particles on the fracture surface finer, thereby enhancing the frictional stability of the rock fracture surface. This finding aligns with previous studies by Verberne et al.[41] and Pluymakers rt al.[42] who reported that the presence of water increases the frictional stability of fault gouge on calcite and gypsum fracture surfaces. Moreover, the cohesion and friction of rock do not act simultaneously[43] and rock undergoes a process of weakening cohesion and strengthening friction during loading failure[44]. The early strength of rock is controlled by cohesion, and the increase in pore water pressure leads to a decrease in cohesion, after which the rock sample enters the plastic stage. The onset of frictional acting is advanced, and the friction angle increases.

Under the same pore water pressure conditions, the cohesion of rock samples increases with temperature; at 40 °C and 55 °C, the increases in cohesion are 1.9% and 3.1%. Conversely, the internal friction angle of
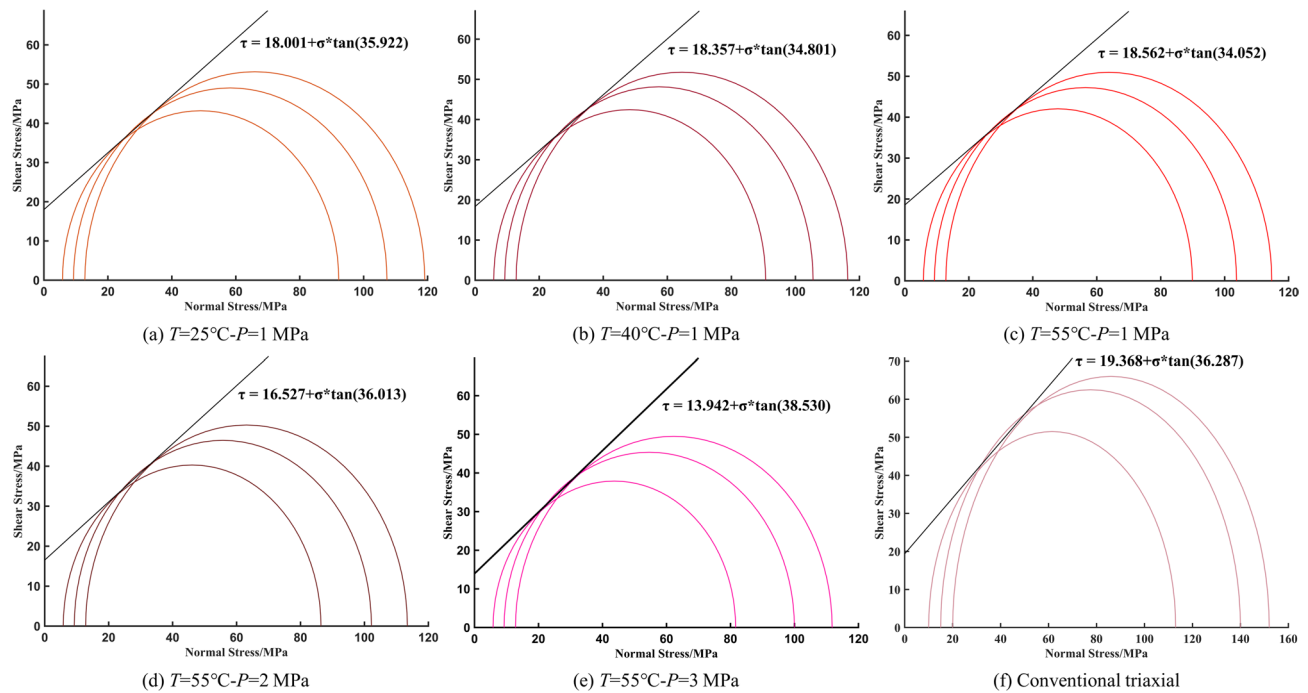
Fig. 10. The Mohr–Coulomb envelopes under different temperatures and pore water pressure.

rock samples decreases with temperature, with reductions of 3.1% and 5.2%. The rise in temperature leads to differential expansion of mineral particles, potentially inducing local thermal stress within the rock and causing cracking due to mismatched thermal expansion at grain boundaries. This may lead to the rapid development of microcracks after the rock sample enters the plastic phase, ultimately resulting in a decrease in the friction angle. Yavuz et al.[45]. have observed calcite separation along grain boundaries due to particle expansion after high temperature exposure.

The sandstone structure and microcracks and their enlarged images are shown in Fig. 11. Electron microscope samples are taken from the fracture surface of each broken sample, and the sample is carefully cut and polished (polished on the back of the fracture). As the temperature increases, the internal structure of the sandstone changes. At 25 °C, the sandstone particles retain their irregular shapes, yet their surfaces become relatively smooth. Obvious holes exist between the particles, but they remain in relatively close contact. There are a few microcracks and holes within the particle structure. When the temperature rises to 40 °C, some particles exhibit slight surface alterations, with their edges and corners becoming more rounded. This may be attributed to the change in interparticle stress resulting from the temperature increase. Notably, the number of micro-cracks between particles increases significantly, and the hole diameters expand as well. At 55 °C, the particles become even more rounded, with more pronounced local deformations. The number and width of micro-cracks increase substantially, and the internal structure appears to be more fragmented.

Research indicates that unloading will amplify the permeability of rocks, and when the temperature surpasses a certain threshold, it encourages microscopic crack initiation. Thus, the permeability failure of sandstone occurs under the combined action of pore water pressure and ground temperature. This characteristic increases the failure risk of surrounding rock in a high hydraulic gradient environment, engineering designs must account for the extent of the unloading loosening circle and the variation in pore water pressure within to assess the bearing capacity and formulate deformation control measures for the unloading zone.

Energy evolution characteristics of the stone failure process
Energy calculation principle
Xie et al.[46] revealed the correlation between energy dissipation and overall failure in the process of rock deformation and failure, emphasizing that rock instability failure is a consequence of energy dissipation and release. It is postulated that all mechanical energy supplied by the testing machine is transformed into the sample's elastic energy and dissipation energy. The elastic energy is conserved within the rock as elastic deformation, which is reversible and can be liberated through deformation upon removal of the external load. Dissipation energy denotes the energy expended by plastic deformation and crack propagation in the rock; this portion of the energy is irreversible[47,48]. Based on Eqs. (5) to (7), the energy relationship during the loading and unloading phases of rock samples under diverse temperatures and pore water pressures is analyzed.

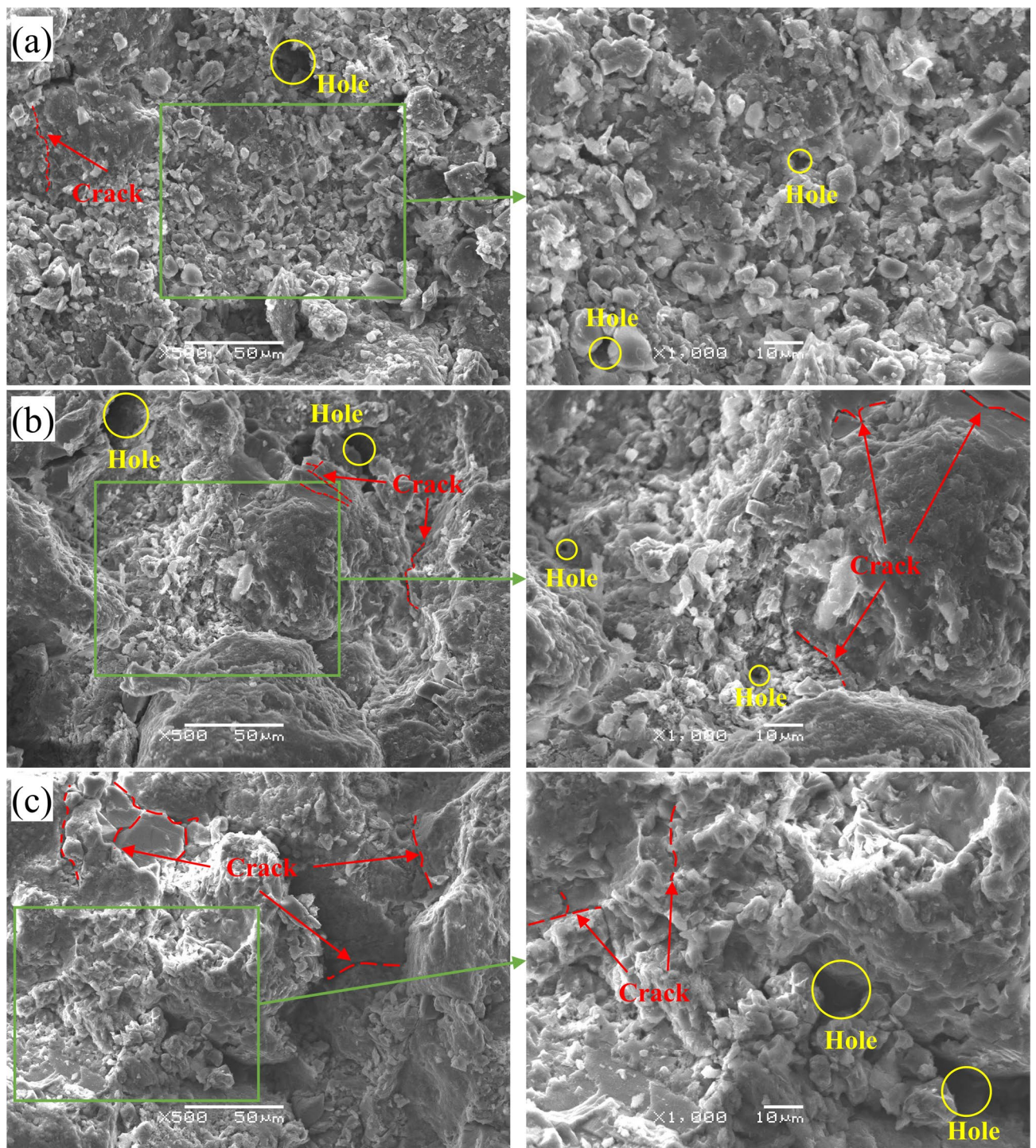$$U = \int_0^{\varepsilon_1} \sigma_1 d\varepsilon_1 + 2 * \int_0^{\varepsilon_3} \sigma_3 d\varepsilon_3 \tag{5}$$

Fig. 11. Microstructure of rock under different temperatures: (**a**) $T = 25\ °C$; (**b**) $T = 40\ °C$; (**c**) $T = 55\ °C$.

$$U = U^e + U^d \tag{6}$$

$$U^e = \frac{1}{2E_0}[\sigma_1^2 + 2\sigma_3^2 - 2\mu(2\sigma_1\sigma_3 + \sigma_3^2)] \tag{7}$$

where U represents the total energy density generated by the external force work during the loading process (MJ/m³); U^e represents the elastic strain energy density (MJ/m³), U^d represents the dissipation energy density (MJ/m³); ε_1 and ε_3 are the axial strain and lateral strain.

Referring to Zhang et al.[49] the elastic modulus during the unloading stage can be approximated by the elastic modulus E_0 from the initial loading phase. Given that lateral deformation is unevenly distributed along the axial direction, typically being more pronounced in the middle and less at both ends, and considering that the circumferential LVDT in the experiment is positioned at the midpoint of the rock sample for measurement, the recorded strain tends to be greater. Consequently, when employing Eq. (5) for calculations, the circumferential strain is considered to be half of the measured value. This study relies on the deviatoric stress-strain curve to construct the energy evolution curve of the rock sample.

Law of energy evolution

As shown in Fig. 12, at the same temperature, with an increase in confining pressure, there is a significant rise in the total energy, dissipation energy, and elastic strain energy of the samples, indicating a pronounced effect of confining pressure. During the loading phase, the rock sample's capacity to absorb more elastic strain energy is enhanced as confining pressure increases, leading to improved energy accumulation in the rock sample. The compaction of the rock sample and the inhibition of lateral deformation by confining pressure effectively restrict energy dissipation and release due to cracking or failure during the unloading phase. Under the influence of pore water pressure, the strength of unloading rock samples is reduced, and deformation is augmented, causing a decline in the total strain energy as pore water pressure increases. Elastic strain energy decreases with higher
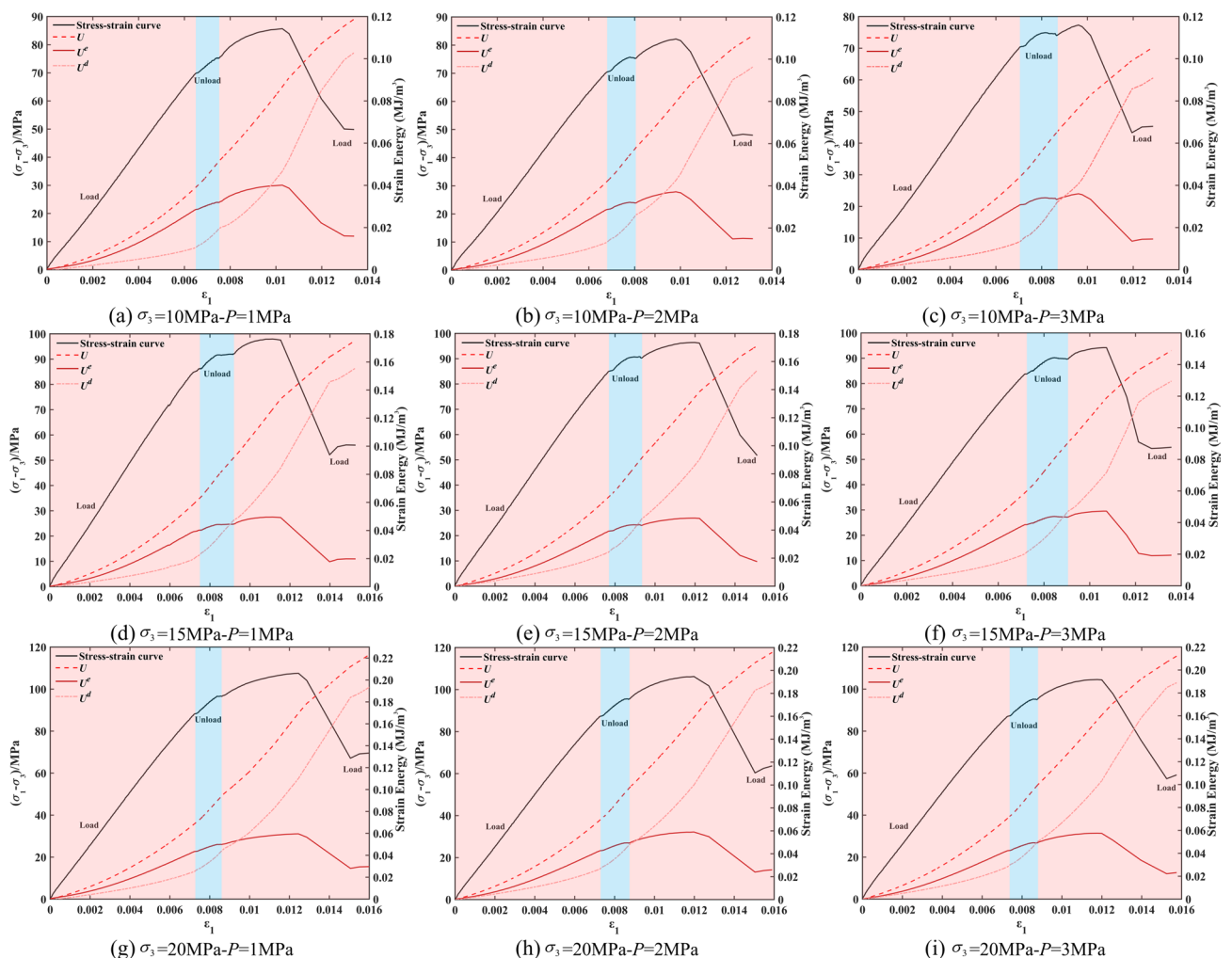

Fig. 12. Energy evolution of the rock failure process under different confining pressures and pore water pressures.
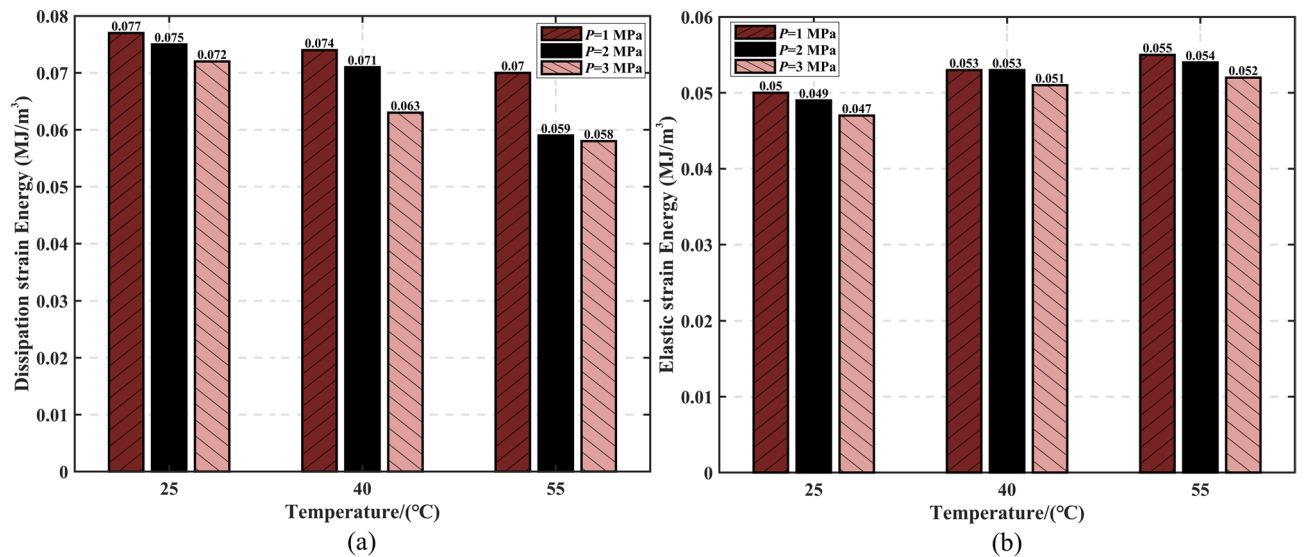
Fig. 13. Energy of sandstone samples at peak points under different temperature and pore water pressures: (**a**) dissipation energy; (**b**) elastic energy.
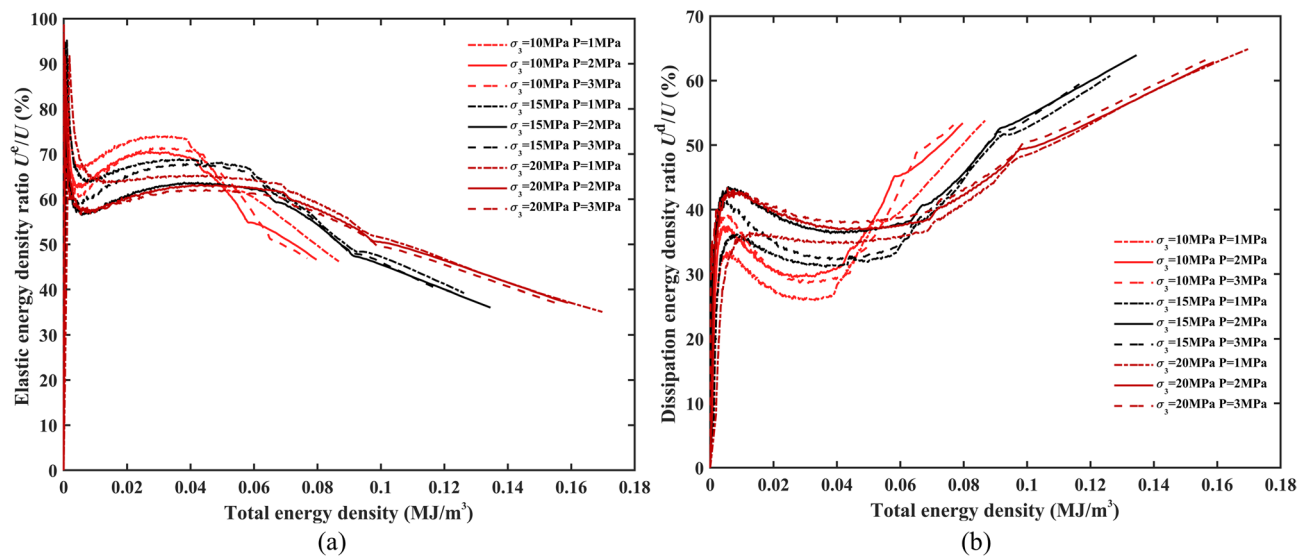

Fig. 14. The pre-peak energy ratio of sandstone: (**a**) dissipated energy ratio; (**b**) elastic energy ratio.

pore water pressure, and dissipation energy generally exhibits a downward trend with the rise in pore water pressure. Damage from unloading-induced expansion in rocks leads to the extensive development of internal fractures and a steep increase in dissipation energy. Elevated pore water pressure promotes crack propagation; thus, the higher the pore water pressure, the less energy is needed for rock failure[13], and correspondingly, the stored elastic strain energy decreases.

As shown in Fig. 13, under the same confining pressure, the bearing capacity of the rock samples decreases with increasing temperature, and the peak strain decreases, resulting in a reduction in both the total strain energy and the stored elastic strain energy. When the temperature is higher, the change in dissipated energy caused by pore water pressure variation becomes more significant. The analysis suggests that the temperature rise causes internal particle expansion, and under thermal stress, the number and width of microcracks in the samples increase, reducing the contact area between sandstone particles, accelerating the strength degradation of the rock samples, and leading to accelerated rock failure.

Figure 14 shows the pre-peak energy ratio of sandstone at the initial stage of loading. Due to the existence of natural micro-cracks and pores in the rock, the transmission of force during loading is complex, resulting in a high proportion of dissipated energy in the input energy. This results in fluctuations in the dissipative energy proportion and elastic energy proportion curves under various test conditions. With the increase of axial force,

the mineral particle extrusion leads to the gradual compaction of the rock sample, and the dissipated energy proportion gradually decreases.

During the confining pressure unloading stage, the axial pressure remains constant, and the reduction of confining pressure leads to the rapid development of microcracks within the rock, causing the proportion of dissipated energy to shift from decreasing to increasing. After the confining pressure unloading stage ends, the proportion of dissipated energy rapidly rises until the rock sample fails, while the change pattern of elastic energy proportion is opposite to that of dissipated energy. As pore water pressure increases, the proportion of dissipated energy shows an upward trend, whereas the input energy decreases with increasing pore water pressure. When the confining pressure increases, the input energy of the rock grows, and the proportion of elastic energy increases accordingly. Higher confining pressure makes the internal particles of the rock more compact, thereby enhancing the rock's resistance to deformation.

Conclusions

(1) Rock unloading expansion provides a pathway for the effects of pore water pressure and temperature. The elastic modulus of rock samples increases with rising temperature and decreases with increasing pore water pressure. The reloading capacity of unloaded rock samples decreases with both increasing pore water pressure and temperature, while confining pressure effectively suppresses rock unloading expansion.

(2) There is a threshold for the effect of pore water pressure on the unloading deformation of sandstone. Under low pore water pressure conditions, rock samples are insensitive to temperature changes. However, under medium to high pore water pressures (2, 3 MPa), unloading deformation exhibits temperature softening characteristics.

(3) Temperature has a minor effect on the shear strength parameters of unloading sandstone, whereas pore water pressure has a significant impact. As pore water pressure increases, the cohesion of the rock decreases while the friction angle increases; at 3 MPa water pressure, cohesion decreases by 24.8%. SEM results show that the number and width of microcracks in sandstone increase with rising temperature.

(4) With increasing pore water pressure, the influence of temperature on the proportion of dissipated energy in sandstone increases. Confining pressure unloading significantly affects the ratio of dissipated energy to elastic energy during rock loading. After confining pressure is unloaded, the proportion of dissipated energy rapidly rises until the rock sample fails under loading.

Data availability

The datasets used and analyzed during the current study available from the corresponding author on reasonable request.

References

1. Hu, S. B., He, L. J. & Wang, J. Y. Heat flow in the continental area of china: a new data set. *Earth Planet. Sci. Lett.* **179**, 407–419. https://doi.org/10.1016/S0012-821X(00)00126-6 (2000).
2. Hu, Y. P., Wang, M. N., Wang, Q. L., Liu, D. G. & Tong, J. J. Field test of thermal environment and thermal adaptation of workers in high geothermal tunnel. *Build. Environ.* **160**, 106174. https://doi.org/10.1016/j.buildenv.2019.106174 (2019).
3. Hu, Y. P. et al. Research on ventilation cooling design driven by human thermal response in high geothermal temperature tunnel construction. *Case Stud. Therm. Eng.* **61**, 104866. https://doi.org/10.1016/j.buildenv.2019.106174 (2024).
4. Zhang, D. L., Sun, Z. Y. & Fang, Q. Scientific problems and research proposals for Sichuan-Tibet railway tunnel construction. *Undergr. Space*. **7**, 419–439. https://doi.org/10.1016/j.undsp.2021.10.002 (2022).
5. Zhang, G. H. et al. Sources of high-temperature water and gas inrush during tunnel excavation: A case of Bangfu tunnel in Southwest China. *J. Rock. Mech. Geotech. Eng.* **16**, 5027–5049. https://doi.org/10.1016/j.jrmge.2024.01.001 (2024).
6. Cui, P. et al. Scientific challenges in disaster risk reduction for the Sichuan–Tibet railway. *Eng. Geol.* **309**, 106837. https://doi.org/10.1016/j.enggeo.2022.106837 (2022).
7. Hou, T., Yang, X., Xing, H., Huang, K. & Zhou, J. -w. Forecasting and prevention of water inrush during the excavation process of a diversion tunnel at the Jinping II Hydropower Station, China. *SpringerPlus*. **5**, 700. https://doi.org/10.1186/s40064-016-2336-9 (2016).
8. Huang, W., Hu, M., Wang, R., Zhang, J. & Xu, W. Study on Large-Scale Geomechanical experiments on tunnel external water pressure. *Water*. **17** https://doi.org/10.3390/w17070913 (2025).
9. Jiang, Q. et al. Study on the Time-lag failure of sandstone with different degrees of unloading damage. *Periodica Polytechnica-Civil Eng.* **63**, 206–214. https://doi.org/10.3311/PPci.13260 (2019).
10. Li, J. L. *Unloading Rock Mass Mechanics* (China Water and Power, 2003).
11. Xiao, W. J., Zhang, D. M. & Wang, X. J. Experimental study on progressive failure process and permeability characteristics of red sandstone under seepage pressure. *Eng. Geol.* **265**, 105406. https://doi.org/10.1016/j.enggeo.2019.105406 (2020).
12. Zhang, J. W., Song, Z. X. & Wang, S. Y. Mechanical behavior of deep sandstone under high stress-seepage coupling. *J. Cent. South. Univ.* **28**, 3190–3206. https://doi.org/10.1007/s11771-021-4791-x (2021).
13. Liu, X. W. et al. Effects of seepage pressure on the mechanical behaviors and microstructure of sandstone. *J. Rock Mech. Geotech. Eng.* **16**, 2033–2051. https://doi.org/10.1016/j.jrmge.2023.09.010 (2023).
14. Ma, C. Q., Li, H. Z. & Niu, Y. Experimental study on damage failure mechanical characteristics and crack evolution of water-bearing surrounding rock. *Environ. Earth Sci.* **77** https://doi.org/10.1007/s12665-017-7209-1 (2018).
15. Xiao, T. L., Huang, M. & Gao, M. Triaxial permeability experimental study on deformation and failure processes of single-fractured rock specimens. *Shock Vibr.* https://doi.org/10.1155/2020/7329825 (2020).
16. Keshavarz, M., Pellet, F. L. & Loret, B. Damage and changes in mechanical properties of a Gabbro thermally loaded up to 1000℃. *Pure Appl. Geophys.* **167**, 1511–1523. https://doi.org/10.1007/s00024-010-0130-0 (2010).
17. Pathiranagei, S. V. & Gratchev, I. Engineering properties of sandstone heated to a range of high temperatures. *Bull. Eng. Geol. Environ.* **80**, 2415–2432. https://doi.org/10.1007/s10064-020-02065-6 (2021).

18. Qin, M. Z. et al. Microscopic damage evolution and physical-mechanical behavior of high-temperature red sandstone under varying heating and cooling durations. *Sci. Rep.* **15** https://doi.org/10.1038/s41598-025-87925-5 (2025).
19. Rao, Q. H., Wang, Z., Xie, H. F. & Xie, Q. Experimental study of mechanical properties of sandstone at high temperature. *J. Cent. South. Univ. Technol.* **14**, 478–483. https://doi.org/10.1007/s11771-007-0311-x (2007).
20. Kumari, W. G. P. et al. Mechanical behaviour of Australian Strathbogie granite under in-situ stress and temperature conditions: an application to geothermal energy extraction. *Geothermics.* **65**, 44–59. https://doi.org/10.1016/j.geothermics.2016.07.002 (2017).
21. Zuo, J. P., Xie, H. P. & Zhou, H. W. Investigation of meso-failure behavior of rock under thermal-mechanical coupled effects based on high temperature SEM. *Sci. China Phys. Mech. Astronomy.* **55**, 1855–1862. https://doi.org/10.1007/s11433-012-4889-0 (2012).
22. Lu, Y. L., Wang, L. G., Sun, X. K. & Wang, J. Experimental study of the influence of water and temperature on the mechanical behavior of mudstone and sandstone. *Bull. Eng. Geol. Environ.* **76**, 645–660. https://doi.org/10.1007/s10064-016-0851-0 (2017).
23. Meng, T. et al. Evolution of permeability and microscopic pore structure of sandstone and its weakening mechanism under coupled thermo-hydro-mechanical environment subjected to real-time high temperature. *Eng. Geol.* **280**, 105955. https://doi.org/10.1016/j.enggeo.2020.105955 (2021).
24. Bao, X. K. et al. Experimental research on damage characteristics of red sandstone under the combined action of temperature, water and stress. *Sci. Rep.* **14** https://doi.org/10.1038/s41598-024-67833-w (2024).
25. Zhu, D. M., Li, Y. A., Huang, W. C. & Hu, X. W. Experimental study on physico-mechanical responses and energy characteristics of granite under high temperature and hydro-mechanical coupling. *Case Stud. Therm. Eng.* **63**, 105245. https://doi.org/10.1016/j.csite.2024.105245 (2024).
26. Li, M. Y., Wu, Z. J., Weng, L., Zhou, Y. & Liu, Q. Evaluating the pore characteristics of granite in disposal system under thermo-hydro-mechanical (T-H-M) coupling. *Int. J. Rock Mech. Min. Sci.* **160**, 105237. https://doi.org/10.1016/j.ijrmms.2022.105237 (2022).
27. Xu, Y., Xiao, J. J., Li, X., Xia, K. W. & Peng, J. B. Experimental study on the permeability evolution of argillaceous sandstone under elevated temperatures. *Eng. Geol.* **313**, 106974. https://doi.org/10.1016/j.enggeo.2022.106974 (2023).
28. Li, M. Y., Wu, Z. J., Weng, L., Liu, Q. S. & Chu, Z. F. Modelling thermo-hydro-mechanical (THM) effect on the hydro-mechanical properties of granite in disposal system using an improved meso-structure-based DEM model. *Rock Mech. Rock Eng.* **57**, 5129–5154. https://doi.org/10.1007/s00603-024-03779-9 (2024).
29. Li, M. Y. et al. Cross-scale analysis for the thermo-hydro-mechanical (THM) effects on the mechanical behaviors of fractured rock: integrating mesostructure-based DEM modeling and machine learning. *Eng. Fract. Mech.* **306**, 110204. https://doi.org/10.1016/j.engfracmech.2024.110204 (2024).
30. Lei, Q. H., Doonechaly, N. G. & Tsang, C. F. Modelling fluid injection-induced fracture activation, damage growth, seismicity occurrence and connectivity change in naturally fractured rocks. *Int. J. Rock Mech. Min. Sci.* **138**, 104598. https://doi.org/10.1016/j.ijrmms.2020.104598 (2021).
31. Zhang, X. et al. Impact of fracture shear dilation on long-term heat extraction in enhanced geothermal systems: insights from a fully-coupled thermo-hydro-mechanical simulation. *Geothermics.* **96**, 102216. https://doi.org/10.1016/j.geothermics.2021.102216 (2021).
32. Chen, X. Z. et al. Mechanical-characteristic evaluation of excavation unloading rock mass subject to high-temperature conditions. *Eng. Fail. Anal.* **130**, 105757. https://doi.org/10.1016/j.engfailanal.2021.105757 (2021).
33. Kang, P., Zhang, J., Zou, Q. L. & Song, X. Deformation characteristics of granites at different unloading rates after high-temperature treatment. *Environ. Earth Sci.* **79**, 1–11. https://doi.org/10.1007/s12665-020-09088-y (2020).
34. Xiao, F. et al. Effects of high temperature on the mechanical behaviors of sandstone under true-triaxial unloading conditions. *Bull. Eng. Geol. Environ.* **80**, 4587–4601. https://doi.org/10.1007/s10064-021-02205-6 (2021).
35. Tao, M. et al. Evolution of permeability and microscopic pore structure of sandstone and its weakening mechanism under coupled thermo-hydro-mechanical environment subjected to real-time high temperature. *Eng. Geol.* **280**, 105955. https://doi.org/10.1016/j.enggeo.2020.105955 (2021).
36. Wong, T. F. & Brace, W. F. Thermal expansion of rocks: some measurements at high pressure. *Tectonophysics.* **57**, 95–117. https://doi.org/10.1016/0040-1951(79)90143-4 (1979).
37. Huang, S. B. & Yu, S. L. Effect of water saturation on the strength of sandstones: experimental investigation and statistical analysis. *Bull. Eng. Geol. Environ.* **81**, 323. https://doi.org/10.1007/s10064-022-02822-9 (2022).
38. Homand-Etienne, F. & Houpert, R. Thermally induced microcracking in granites: characterization and analysis. *Int. J. Rock Mech. Min. Sci.* **26**, 125–134. https://doi.org/10.1016/0148-9062(89)90001-6 (1989).
39. Pusch, R. Alteration of the hydraulic conductivity of rock by tunnel excavation. *Int. J. Rock Mech. Min. Sci.* **26**, 79–83. https://doi.org/10.1016/0148-9062(89)92562-x (1989).
40. Li, M. H. et al. Permeability evolution of granite under cyclic hydraulic fracturing and its deterioration during in-situ stress retention in geothermal engineering. *Case Stud. Therm. Eng.* **61**, 105043. https://doi.org/10.1016/j.csite.2024.105043 (2024).
41. Verberne, B. A. et al. Frictional properties and microstructure of Calcite-Rich fault gouges sheared at Sub-Seismic sliding velocities. *Pure. Appl. Geophys.* **171**, 2617–2640. https://doi.org/10.1007/s00024-013-0760-0 (2014).
42. Pluymakers, A. M. H., Samuelson, J. E., Niemeijer, A. R. & Spiers, C. J. Effects of temperature and CO2 on the frictional behavior of simulated anhydrite fault rock. *J. Geophys. Res.-Solid Earth.* **119**, 8728–8747. https://doi.org/10.1002/2014jb011575 (2014).
43. Hajiabdolmajid, V., Kaiser, P. & Martin, C. D. Mobilised strength components in brittle failure of rock. *Geotechnique* **53**, 327–336. https://doi.org/10.1680/geot.2003.53.3.327 (2003).
44. Hajiabdolmajid, V. & Kaiser, P. Brittleness of rock and stability assessment in hard rock tunneling. *Tunn. Undergr. Space Technol.* **18**, 35–48. https://doi.org/10.1016/S0886-7798(02)00100-1 (2003).
45. Yavuz, H., Demirdag, S. & Caran, S. Thermal effect on the physical properties of carbonate rocks. *Int. J. Rock Mech. Min. Sci.* **47**, 94–103. https://doi.org/10.1016/j.ijrmms.2009.09.014 (2010).
46. Xie, H. P., Li, L. Y., Peng, R. D. & Ju, Y. Energy analysis and criteria for structural failure of rocks. *J. Rock Mech. Geotech. Eng.* **1**, 11–20. https://doi.org/10.3724/SP.J.1235.2009.00011 (2009).
47. Wang, Z. F., Qi, C. Z., Zhao, F., Jiang, K. & Feng, Y. J. A new critical strain energy release rate failure criterion for anisotropic rock under high confining pressure. *Geomech. Energy Environ.* **34**, 100464. https://doi.org/10.1016/j.gete.2023.100464 (2023).
48. Fu, J. J., Wang, Z. L., Wang, J. G., Feng, C. C. & Li, S. Y. The energy evolution and constitutive model of layered rock at medium and high strain rates. *Environ. Earth Sci.* **84**, 93. https://doi.org/10.1007/s12665-024-12052-9 (2025).
49. Zhang, L. M. et al. Energy evolution analysis and failure criteria for rock under different stress paths. *Acta Geotech.* **16**, 569–580. https://doi.org/10.1007/s11440-020-01028-1 (2021).

Author contributions

S.G.: Methodology, validation, formal analysis, writing-original draf, writing–review, data curation. X.C.: Supervision, funding acquisition, conceptualization, writing-review and editing. L.C.: Investigation, writing-review and editing. Z.L.: Writing-review and editing.

Funding

Declarations

Competing interests
The authors declare no competing interests.

Additional information
Correspondence and requests for materials should be addressed to X.C.

Reprints and permissions information is available at www.nature.com/reprints.

Publisher's note Springer Nature remains neutral with regard to jurisdictional claims in published maps and institutional affiliations.